Journal of Power Sources 195 (2010) 8116–8123

Contents lists available at ScienceDirect

Journal of Power Sources

journal homepage: www.elsevier.com/locate/jpowsour

Co-precipitation in aqueous medium of $La_{0.8}Sr_{0.2}Ga_{0.8}Mg_{0.2}O_{3-\delta}$ via inorganic precursors

Renato Pelosato[a,*], Cinzia Cristiani[a], Giovanni Dotelli[a], Saverio Latorrata[a], Riccardo Ruffo[b], Luca Zampori[a]

[a] CMIC - Dipartimento di Chimica, Materiali e Ingegneria Chimica "G. Natta", Politecnico di Milano, P.zza Leonardo da Vinci 32, 20133 Milano, Italy
[b] Dipartimento di Scienza dei Materiali, Università di Milano-Bicocca, Via Cozzi 53, 20125 Milano, Italy

ARTICLE INFO

Article history:
Received 7 May 2010
Received in revised form 7 July 2010
Accepted 18 July 2010
Available online 22 July 2010

Keywords:
SOFCs
LSGM
Co-precipitation
Characterization

ABSTRACT

A simple and inexpensive co-precipitation route in aqueous medium is proposed to prepare $La_{0.8}Sr_{0.2}Ga_{0.8}Mg_{02}O_{3-\delta}$ ionic conductor (LSGM). Different synthetic procedures and operating parameters (i.e. nature and amount of the precipitating agents, HNO_3 addition and temperature) have been evaluated in order to underline their influence on the composition and microstructure of the final phase. Intermediate and final products were characterized by Thermal-Gravimetry, IR-spectroscopy, X-ray Powder Diffraction, Rietveld analysis and Scanning Electron Microscopy. The electrical properties were measured by Impedance Spectroscopy in the temperature range 250–800 °C. Slight variations of the synthetic procedure (such as precipitating agent amount or no HNO_3 addition) have a considerable and detrimental effect on the ions losses and the subsequent achievement of the final phase. The use NH_4OH as an alternative precipitating agent is dramatically disadvantageous. Ions losses during precipitation must be controlled (i) to avoid understoichiometry in the LSGM phase and (ii) to prevent the formation of large amounts of secondary phases. In fact, both affect the total electrical conductivity.

The use of large excess of $(NH_4)_2CO_3$ precipitating agent and the addition of HNO_3 lead to the best material characterized by a rhombohedral structure, small amount of side phases, a relative density of 98% and a total conductivity of 6.44×10^{-2} S cm^{-1} at 800 °C and 1.13×10^{-2} S cm^{-1} at 600 °C.

1. Introduction

Solide Oxide Fuel Cells (SOFCs) are electrochemical devices combining the benefits of environmentally friendly power generation with fuel flexibility. At present, Yttria Stabilized Zirconia (YSZ), which operates at 900–1000 °C, is widely used as the electrolyte in SOFCs. However, the significant advantages of such high-*T* SOFCs are accompanied by drawbacks, the most important of which is materials durability. In this respect, operating at lower temperatures is of evident interest. Accordingly, a great effort has been done in developing alternative materials and systems able to operate in the temperature range 650–800 °C. Among alternative electrolytes, perovskite oxides with the formula $La_{1-x}Sr_xGa_{1-y}Mg_yO_{3-\delta}$ are reported to have fast ionic transport, wide electrolytic domain and chemical stability in both oxidant and reducing environments [1,2].

The phase diagram of the La_2O_3–SrO–Ga_2O_3–MgO system is quite complex, and several two and three-component side phases are in thermodynamic equilibrium with the main phase up to 1400 °C. Thus, the chance of using LSGM as electrolyte in intermediate temperature SOFC lies in its metastability [3]. To investigate the phase development in the complex multi-oxide system and to obtain pure and fully dense perovskite material, several synthetic routes have been adopted for the preparation of LSGM, with alternate results. Among the most common, the classic solid-state reactive firing with oxides and carbonates precursors [1,2,4–7] and a large assortment of Pechini-type and sol–gel/wet-chemistry methods and processes [3,8–20]; other isolated attempts include hydrothermal methods [21], and self-propagating high-temperature synthesis [22]. However, many of these routes have problems in process scalability or cost, and some are very time-consuming or require special equipments or severe experimental conditions. Even if LSGM can be obtained with special synthetic routes at low-temperature (as low as 900 °C according to Chen and Fung [21]), dense samples can be obtained only after high-temperature sintering [23]. $La_{1-x}Sr_xGa_{1-y}Mg_yO_{3-\delta}$ conductivity increases with doping amount up to a maximum when $x \approx y \approx 0.16$–0.20 where the solubility limits of Sr and Mg in the lattice are reached [24]. For what concerns the crystal structure, if we rely on the most accurate determinations allowed by

* Corresponding author. Tel.: +39 02 2399 3232; fax: +39 02 7063 8173.
E-mail address: renato.pelosato@chem.polimi.it (R. Pelosato).

0378-7753/$ – see front matter © 2010 Elsevier B.V. All rights reserved.
doi:10.1016/j.jpowsour.2010.07.046

neutron diffraction and synchrotron experiments, the following situation is depicted: the undoped perovskite $LaGaO_3$ crystallizes in orthorhombic *Pbnm* space group [25–27]; when $(x+y) \leq 0.2$ LSGM crystal structure has been reported as orthorhombic in two different space groups, *Ibmm* [28–30] or *Imma* [31,32]. The structure shifts to monoclinic *I2/a* [25,27–29] or orthorhombic *Imma* [30] for $0.2 \leq (x+y) \leq 0.3$ [31]. For a total amount of dopants $(x+y) > 0.3$ most authors report a cubic structure [26,32,33]. Nevertheless, some others as Rozumek et al. [3] report a rhombohedral structure obtained by Rietveld refinements of a laboratory X-ray pattern, and Idemoto et al. [34] claim an orthorhombic *Pnma* structure on the basis of neutron diffraction studies.

In this work an alternative, simple and inexpensive preparation method by co-precipitation in aqueous medium is proposed [35,36]; the variability of the structure of LSGM with the dopant concentration and the intrinsic complexity of the precipitation equilibria of many species are possibly the reasons that delayed the use of co-precipitation methods for the synthesis of LSGM electrolytes until very recent years [37–39]. Indeed, co-precipitation in aqueous medium can sometimes suffer of incomplete precipitation of some species, leading to incorrect final stoichiometry. This easily happen when many species are involved, and depends on the nature of the cations and experimental conditions. In the case of LSGM this drawback could be particularly critical, given the dependence of the conductivity on the dopant stoichiometry. Even replenishment of the lost species with successive solid-state reaction [39] has been proposed, but it does not sound convincing as the advantages of wet-chemistry processes are clearly lost.

In the present work, different synthetic procedures have been evaluated to apply a co-precipitation route in aqueous medium in the synthesis of LSGM. Simple precipitating agents (namely ammonium carbonate and ammonium hydroxide) were used, and slight variations of the standard procedure have been investigated in order to understand the factors influencing the final precipitation yield and therefore the final phase composition and microstructure of the products. Intermediate and final products were also characterized by Thermal-Gravimetry, IR-spectroscopy, X-ray Powder Diffraction and Scanning Electron Microscopy. The electrical properties of obtained LSGMs were measured by Impedance Spectroscopy in the temperature range 250–800 °C.

2. Experimental

Precursors used in the co-precipitation in aqueous medium were $La(NO_3)_3{\cdot}6H_2O$ (99.99%, Sigma Aldrich), $Ga(NO_3)_3{\cdot}xH_2O$ (99.999%, Sigma Aldrich, $x = 7$ from manufacturer analysis) $Mg(NO_3)_3{\cdot}6H_2O$ (99.999%, Sigma Aldrich), $Sr(NO_3)_3$ (99.9%, Sigma Aldrich, anhydrous), $(NH_4)_2CO_3$ (99.999% Sigma Aldrich), NH_4OH (28%, w/w, 99.99%, Sigma Aldrich), HNO_3 (65%, w/w, Sigma Aldrich), distilled water. In a typical experiment, stoichiometric amounts of La, Sr, Ga and Mg nitrates were dissolved in water at 60 °C with a total metal ion concentration of about 1 M; HNO_3 was added to prevent the precipitation of the ions at this stage.

Simultaneously, the precipitating agent was dissolved in a jacked reactor, keeping the temperature constant at 60 °C with a thermostat, to assure the decomposition of the carbammates when the commercial ammonium carbonate was used. A condenser using tap water as coolant was used to avoid volume variation during the reaction.

The nitrates solution was poured in the precipitating agent one under vigorous stirring and an immediate precipitation was observed. The so formed suspension was aged for 3 h at 60 °C to allow the complete precipitation. At the end of the ageing time the suspension was filtered under N_2 pressure using Durapore® GVHP 14,250 membranes with pore size of 0.22 μm. The cake was washed up to nitrates disappearance and dried at 110 °C overnight under strong recirculation of air. The mother liquors were collected and analyzed to check the presence of remaining ions by Atomic Absorption equipment (Varian AA 110 instrument, internal standard method).

The dried powders were crushed in a mortar, fired at 1000 °C and 1400 °C for 10 h (heating/cooling rate = 1 °C min^{-1}) under strong recirculation of air. Characterization of samples was performed by X-ray Powder Diffraction (XRPD) with a Bruker D8 instrument using graphite monochromated Cu-K_α radiation; the diffraction patterns were collected in the range 10–80° 2θ with a step of 0.02° 2θ and a counting time of 12 s per step. Infrared Spectroscopy (FT-IR) was performed using a JASCO FT/IR-615 spectrophotometer and a Carl Zeiss EVO 50VP Scanning Electron Microscopy (SEM) equipped with EDS. Powders fired at 1400 °C were analyzed by Rietveld refinements of the XRPD data using the GSAS software package [40] to attain structural information and quantitative phase composition. Pellets fired at 1400 °C were used for the Impedance Spectroscopy (IS) characterization. Pt painted current collectors were applied on both faces of the sintered pellets and then fired at 850 °C for 1.5 h; some authors reported slight interaction between Pt and LSGM during cell tests, both in reducing [41] and oxidizing [42] environments, but in our measurements we did not have any evidence suggesting such reactivity. The density of the powder was determined by the Archimedes method; due to the complex phase composition, the relative density ρ of each sample was calculated using the following equation:

$$\rho = \frac{\rho^{\exp}}{\sum_{i=1}^{n}(f_i \times \rho_i^{\text{th}})}\% \quad (1)$$

where $\rho^{\exp}$ is the measured density, f_i the volume fraction of phase i, ρ_i^{th} its theoretical density calculated from the refined lattice parameters and n the number of the phases.

The stoichiometric amount of the precipitating agent was calculated hypothesizing some simple precipitation reactions (Table 1) where only pure carbonates or hydroxides are formed. The formation of double- or multi-metal compounds was excluded at this stage for simplicity.

To evaluate the effect of the reaction conditions and the nature of the precipitating agent on the composition of the final precipitate, four different synthetic procedures were evaluated, named *P*1, *P*2, *P*3 and *P*4, respectively; here follows the experimental details of each preparation:

P1 (HNO_3 – excess carbonate): nitric acid was added to the metal nitrates solution until pH = 1. The precipitating agent, $(NH_4)_2CO_3$, was dissolved in water (concentration 2 M) in a 20% excess, calculated on the reaction scheme of Table 1. Precipitation was achieved by pouring the nitrate solution into the ammonium carbonate one. The final pH was 6.5–7.

Table 1
Hypothesized reaction scheme for co-precipitation with $(NH_4)_2CO_3$ (left) and NH_4OH (right).

Precipitating agent: $(NH_4)_2CO_3$	Precipitating agent: NH_4OH
$3(NH_4)_2CO_3 + 2La^{3+} \rightarrow La_2(CO_3)_3 + 6NH_4^+$	$3NH_4OH + La^{3+} \rightarrow La(OH)_3 + 3NH_4^+$
$(NH_4)_2CO_3 + Sr^{2+} \rightarrow SrCO_3 + 2NH_4^+$	$2NH_4OH + Sr^{2+} \rightarrow Sr(OH)_2 + 2NH_4^+$
$3(NH_4)_2CO_3 + Ga^{3+} + 3H_2O \rightarrow Ga(OH)_3 + 6NH_4^+ + 3HCO_3^-$	$3NH_4OH + Ga^{3+} \rightarrow Ga(OH)_3 + 3NH_4^+$
$(NH_4)_2CO_3 + Mg^{2+} \rightarrow MgCO_3 + 2NH_4^+$	$2NH_4OH + Mg^{2+} \rightarrow Mg(OH)_2 + 2NH_4^+$

Table 2
Ion losses (ion concentration measured by AAS in the mother liquors).

Sample	Ion losses (mol%)				Expected stoichiometry from ion losses	$x+y$
	La	Sr	Ga	Mg		
Theoretical	–	–	–	–	$La_{0.80}Sr_{0.20}Ga_{0.80}Mg_{0.20}O_{3-\delta}$	0.40
*P*1	<0.1	<0.1	3.6	21	$La_{0.80}Sr_{0.20}Ga_{0.77}Mg_{0.16}O_{3-\delta}$	0.36
*P*2	<0.1	0.2	<0.1	6	$La_{0.80}Sr_{0.20}Ga_{0.80}Mg_{0.19}O_{3-\delta}$	0.39
*P*3	<0.1	51	0.4	77	$La_{0.80}Sr_{0.10}Ga_{0.80}Mg_{0.05}O_{3-\delta}$	0.15
*P*4	<0.1	100	4.3	9.9	$La_{0.8}Ga_{0.77}Mg_{0.18}O_{3-\delta}$	0.18

P2 (HNO_3 – stoichiometric carbonate): nitric acid was added to the metal nitrates solution until pH = 1. The precipitating agent, $(NH_4)_2CO_3$ was dissolved in water (concentration 2 M) in the theoretical stoichiometric ratio according to reactions in Table 1. Precipitation was achieved by pouring the metal nitrate solution into the ammonium carbonate one. The final pH was 6.5–7.

P3 (no HNO_3 – excess carbonate): no nitric acid was added to the metal nitrate solution, that kept a starting pH of 2. The precipitating agent, $(NH_4)_2CO_3$ was dissolved in water (concentration 2 M) in a 20% excess, calculated on the reaction scheme of Table 1. Precipitation was achieved by pouring the nitrate solution into the ammonium carbonate one. The precipitation pH was about 7.

P4 (HNO_3 – stoichimetric ammonia): nitric acid was added to the metal nitrates solution until pH = 1. The precipitating agent was NH_4OH (5 M), in the theoretical stoichiometric ratio (according to reactions in Table 1). Precipitation was achieved by pouring the metal nitrate solution into the ammonium carbonate one. The final pH was about 8.5.

3. Results and discussion

3.1. Ion losses

The mother liquors were collected after filtration and analyzed for the presence of non-precipitated ions. Results are reported in Table 2 as mol%. The respective expected compositions of the final phase, calculated under the hypothesis of the formation of a final single phase sample, are also reported. The samples fired at 1400 °C were analyzed for their metal content via AA analyses of the powders. Given the presence of secondary phases, the results of chemical analysis of samples *P*1, *P*2 and *P*3 cannot be directly correlated to the stoichiometry of the final perovskite phase; however, in the case of *P*4, which is single phase, the analysis of the solid confirm the results obtained for mother liquors.

Using NH_4OH as precipitating agent Sr is completely retained in solution and lost during the filtration step, and also part of Mg and Ga ions are found in the mother liquors (procedure *P*4, Table 2). The resulting calculated stoichiometry lacks of more than half of the desired dopants concentration: for *P*4, a very poorly doped sample, $(x+y) = 0.18$ is found in comparison with $(x+y) = 0.4$ of the theoretical value. Thus the use of NH_4OH as precipitating agent is not recommended.

Procedure *P*3 (no addition of HNO_3 in the starting nitrates solution) also leads to massive ion losses, more equally distributed between the two dopants. Also in this case the calculated stoichiometry for the expected conductive phase lacks more than half of the desired dopants concentration ($x+y = 0.15$).

Ion losses are much decreased in samples *P*1 and *P*2 synthesized by pouring an acidificated solution of the metal nitrates in the $(NH_4)_2CO_3$ one. In *P*1, where an excess of precipitating agent (about 20 wt%) was present, a considerable loss of magnesium (21%) was observed. Sr ions loss was below the detection limits of the instrument and only a small amount of Ga was revealed in the mother liquors. Accordingly, the desired stoichiometry was nearly retained ($x+y = 0.36$).

When the precipitating agent was stoichiometric (*P*2), no major losses were observed, but minor amounts of Mg (6%) and Sr (0.2%) were detected in the mother liquors, and the deviation from the desired stoichiometry was the smallest ($x+y = 0.39$).

3.2. Phase composition and crystal structure

Phase composition has been studied by X-ray Powder Diffraction (XRPD) on grinded powders fired at different temperatures. Diffraction patterns were collected after treatment at 110 °C (precipitated samples overnight dried), 1000 °C (calcination step) and 1400 °C (sintering step). On the highest temperature samples, Rietveld analysis was performed on X-ray data to obtain the exact phase composition of the sample and the crystal structure of the final perovskite phase. Results of qualitative and quantitative XRD analysis are summarised in Table 3.

Table 3
Phase composition of the samples from XRD (110, 1000 and 1400 °C (P, perovskite; Am, amorphous).

Sample	Phase composition (qualitative, XRD)		Phase composition (quantitative, XRD)
	110 °C	1000 °C	1400 °C
*P*1	$Mg(OH)_2$ $SrCO_3$ Am	P $La_4Ga_2O_9$ $LaSrGaO_4$ $LaSrGa_3O_7$	83% P 16% $LaSrGaO_4$ 1% $LaSrGa_3O_7$
*P*2	$Mg(OH)_2$ $SrCO_3$ Am	P $La_4Ga_2O_9$ $LaSrGaO_4$ $LaSrGa_3O_7$	54% P 43% $LaSrGaO_4$ 3% $LaSrGa_3O_7$
*P*3	$La_2(CO_3)_2(OH)_2$ $Mg(OH)_2$ Am	P $La_4Ga_2O_9$ $LaSrGa_3O_7$	89% P 11% $La_4Ga_2O_9$
*P*4	$La(OH)_3$ Am	P	100% P

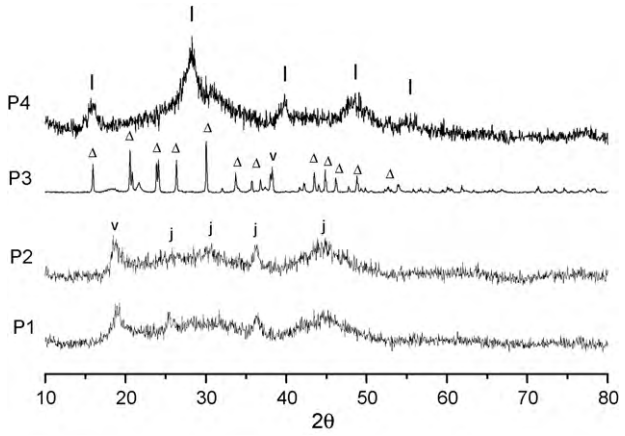

Fig. 1. XRD patterns of co-precipitated samples after drying at 110 °C (symbols l = $La(OH)_3$; Δ = $La_2CO_3 \cdot 2(OH)_2$; v = $Mg(OH)_2$; j = $SrCO_3$).

3.2.1. Dried samples (110 °C overnight)

The XRPD diffraction patterns of the dried samples are reported in Fig. 1. Samples *P*1, *P*2 and *P*4 show a mixture of crystalline and amorphous phases, while sample *P*3 shows mainly crystalline phases. The identified microcrystalline phases are $Mg(OH)_2$ (JCPDS #07-0239) and $SrCO_3$ (JCPDS #05-0418) in *P*1 and *P*2, $La_2(CO_3)_2(OH)_2$ (JCPDS #28-0512) and $Mg(OH)_2$ in *P*3, and mainly $La(OH)_3$ (JCPDS #36-1481) in *P*4 (Table 3).

TG analyses up to 1000 °C (Fig. 2a) shows a progressive weight loss of about 20–30% (w/w) for all the samples. The observed weight losses occur via three decomposition steps that can be associated with hydroxides, hydroxycarbonates and/or carbonates decompositions either for temperatures and extent [35]. Further weight losses are no longer detectable at temperatures higher than 900 °C meaning that the precursors are totally decomposed.

Despite the close temperature range of the precursors decomposition, different behaviors are observed (Fig. 2b) in DTG. In the case of *P*2, in fact, the decomposition phenomena are completed at about 800 °C, while in the case of *P*1 and *P*3, the completion of the reactions is observed 50–100 °C above. Therefore, it can be inferred that the *P*2 precursors are easier to decompose.

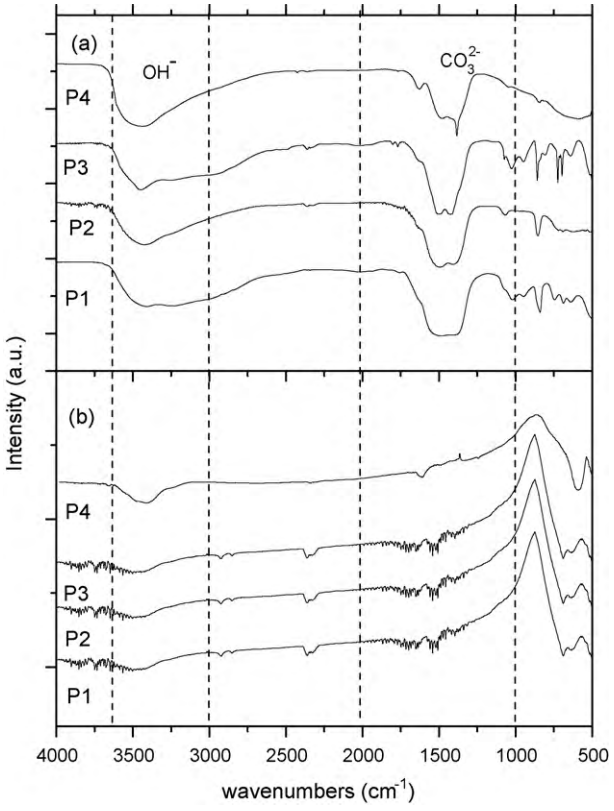

Fig. 3. FT-IR spectra of: (a) the as-synthesized powders dried at 110 °C and (b) fired at 1400 °C.

In the FT-IR spectra of the dried precursors (Fig. 3a) the presence of carbonate and hydroxycarbonates are confirmed by the characteristic bands at 1492, 1386, 1067 and 850 cm^{-1} and by the hydroxides band at 3500 cm^{-1}. Sample *P*4, prepared using ammonia as precipitating agent, shows, together with the OH band at

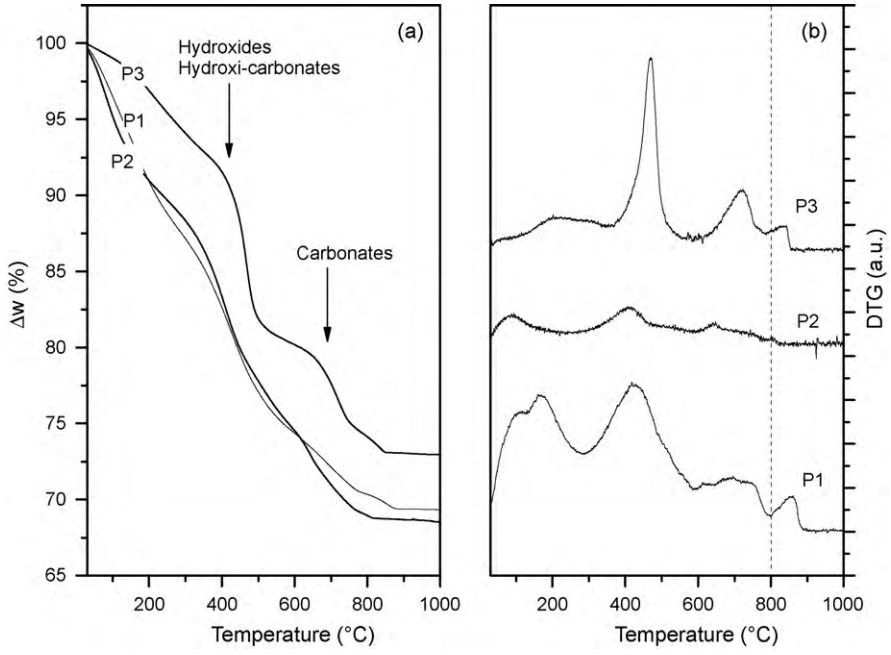

Fig. 2. Thermogravimetric analysis of the *P*1, *P*2, *P*3 precursors dried at 110 °C.

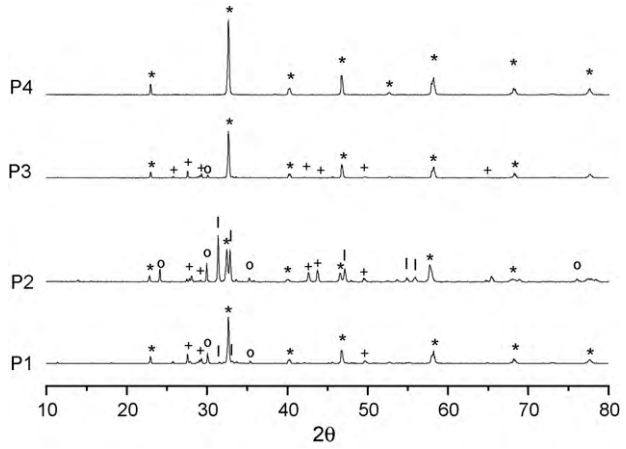

Fig. 4. XRD patterns of co-precipitated samples fired at 1000 °C (symbols: * = Perovskite; + = $La_4Ga_2O_9$; O = $LaSrGa_3O_7$; | = $LaSrGaO_4$).

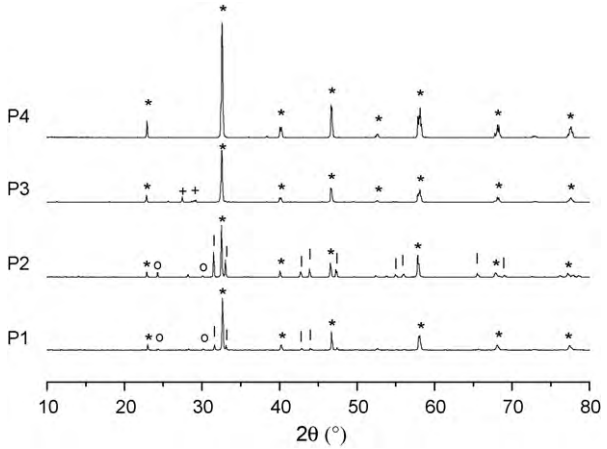

Fig. 5. XRD patterns of co-precipitated samples fired at 1400 °C (symbols: * = Perovskite; + = $La_4Ga_2O_9$; O = $LaSrGa_3O_7$; | = $LaSrGaO_4$).

3500 cm^{-1}, the typical N–H band at around 1400 cm^{-1} due to residual ammonia [43].

3.2.2. Thermal treatments at 1000 and 1400 °C

In line with TG results on precursors, the perovskite phase is already formed at 1000 °C in all samples (Fig. 4), and, except for sample *P*2, it always appears as the most abundant phase. Common ternary side phases, such as $LaSrGaO_4$ (JCPDS #80-1806), $LaSrGa_3O_7$ (JCPDS #45-0637) and $La_4Ga_2O_9$ (JCPDS #37-1433), are identified in the diffraction patterns of *P*1, *P*2 and *P*3, while only the perovskite is found in sample *P*4. As inferred by the ion losses analyses (Table 3), sample *P*4 is poorly doped thus it already develops a pure perovskite phase at lower temperatures, as in fact has been observed by the authors on a undoped $LaGaO_3$ reference sample prepared using the same procedure. The complete decomposition of non-oxide species is confirmed by the disappearance of the hydroxides and carbonates signals in the FT-IR spectra recorded on powders sintered at 1400 °C (Fig. 3b).

The XRD spectra of the samples sintered at 1400 °C (Fig. 5) were refined with the Rietveld method starting from literature model structures, to evaluate the crystal structure of the Perovskite phase and the quantitative phase composition (Fig. 6, Tables 3 and 4). On the basis of the residue stoichiometry of the dopants, a rhombohedral model for the perovskite structure was hypothesized for *P*1

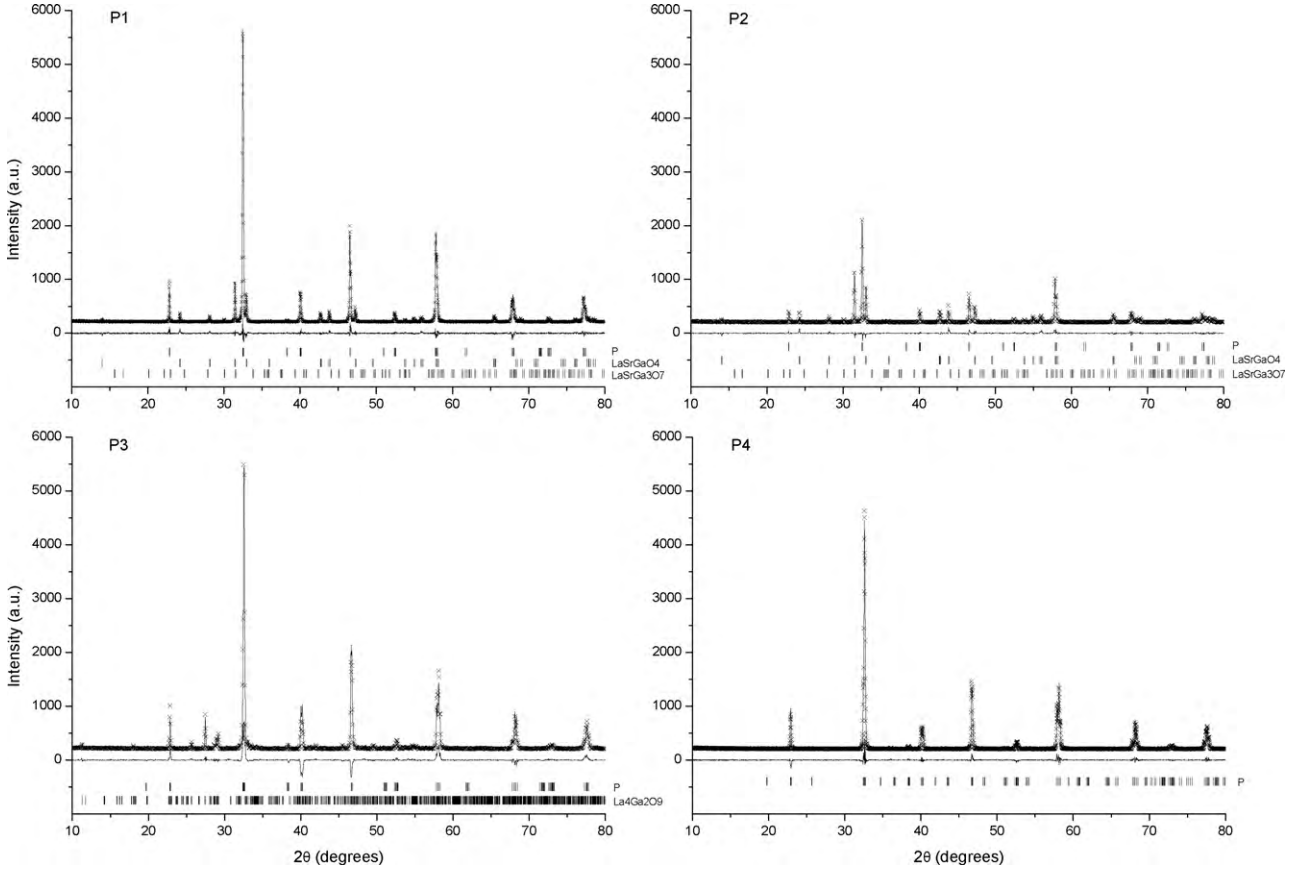

Fig. 6. Rietveld refinements of *P*1, *P*2, *P*3 and *P*4; (*x* = experimental, line = calculated, bottom line = difference, | = peak positions).

Table 4
Results of Rietveld analysis on samples sintered at 1400 °C.

	*P*1	*P*2	*P*3	*P*4
Crystal system	R	R	O	O
Space group	R-3c	R-3c	*Imma*	*Pbnm*
a (Å)	5.5315 (3)	5.5338 (3)	5.4895 (4)	5.5321 (2)
b (Å)	5.5315 (3)	5.5338 (3)	7.7743 (6)	5.4942 (2)
c (Å)	13.5157 (13)	13.551 (2)	5.5261 (4)	7.7821 (2)
α	90	90	90	90
β	90	90	90	90
γ	120	120	90	90
V (Å^3)	358.14 (5)	359.378 (5)	235.84 (4)	236.53 (2)
Tolerance factor	0.995	0.995	1.03	0.963
Z	6	6	4	4
χ^2	1.851	1.649	3.919	1.471
Structural model	Kajitani et al. [28]		Guenter et al. [30]	Kajitani et al. [32]

and *P*2 according to Kajitani et al. [28] while an orthorhombic one for *P*3 and *P*4 following the models in Refs. [30,32], respectively. An attempt to fit the experimental data with the cubic model reported for pure LSGM8282 in Ref. [32] was unsuccessful.

Upon sintering at 1400 °C 10 h, the perovskite formation reaction proceeds at the expense of the side phases and the perovskite becomes the dominant phase for all the samples (Table 3). High perovskite phase percentage, 83–89 wt% are calculated for samples *P*1 and *P*3, while in *P*2 sample large amount of side phases are retained (54 wt% of perovskite) (Fig. 4, Table 3). Furthermore, the Rietveld refinements have been successfully fitted with the hypothesized structural models, with χ^2 in the range 1.47–3.92 obtained for all the samples (Fig. 6, Table 4) that confirms the deviation from the cubic structure. The discrepancy between nominal and actual stoichiometry may be also responsible for the presence of the side phases at all the temperatures. Ion losses during precipitation, in fact, result in metal ratios that could not account for the composition of the theoretical cubic perovskite. Thus, excess ions, that cannot be allocated in the rhombohedral or the orthorhombic structures, segregate as side phases.

The understanding of the behavior of *P*2 sample when compared with *P*1 is not trivial, and needs some supplementary analysis. *P*2 shows the lowest cumulated ions losses (Table 1), but the highest amount of secondary phases in the sample after sintering at 1400 °C (Fig. 5 and Table 3).

According to TG-DTG data discussed above, it can be hypothesized a difference in the phase composition of the precipitated precursors (for example, a carbonate rich vs. an hydroxide rich composition). These different precursors likely decompose at different temperatures, as shown by the TGs of *P*1 and *P*2, where the complete decomposition of the non-oxide phases is observed at 900 and 800 °C for *P*1 and *P*2, respectively (Fig. 2b). In that case, the earlier the 'non-oxide' species are decomposed, the earlier the side phases, thermodynamically more stable than the doped perovskite phase at $T < 1500$ °C [3], can be formed. Once formed, these phases can progressively crystallize during the thermal treat-

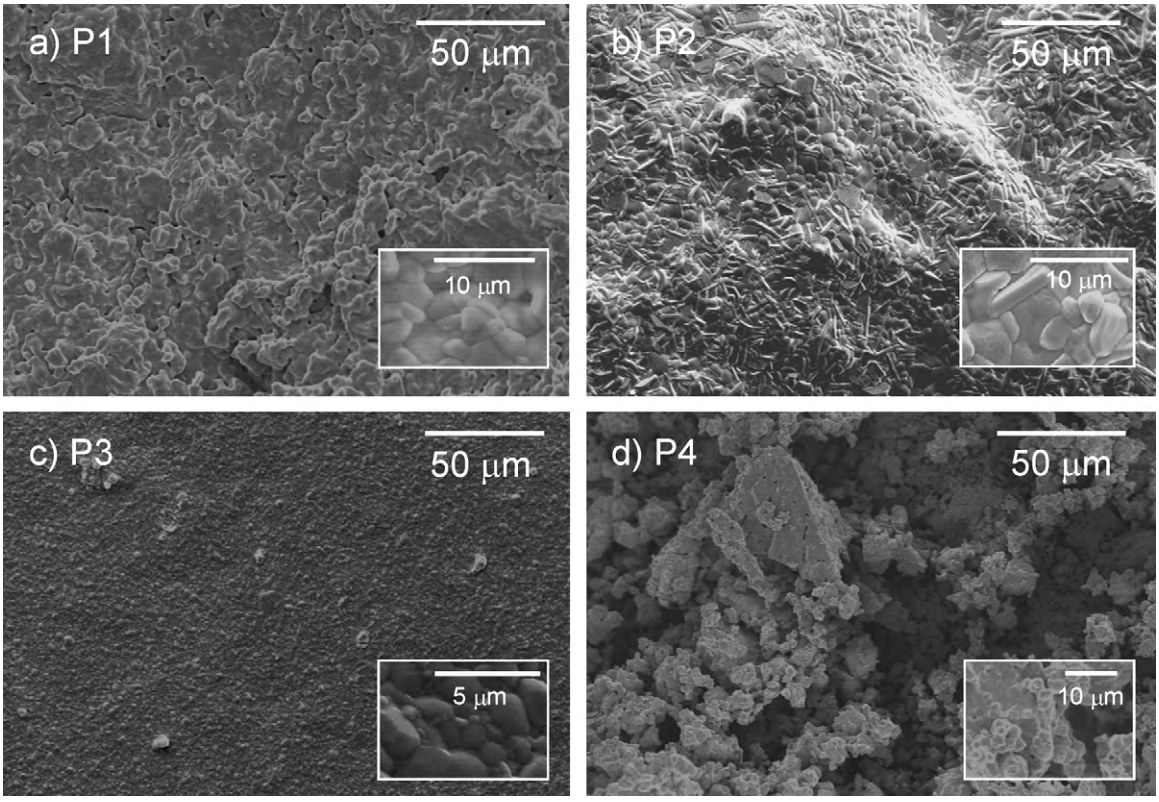

Fig. 7. Secondary Electron SEM micrographs of samples *P*1 (a), *P*2 (b), *P*3(c) and *P*4(d) with insets at higher magnification.

Table 5
Total electrical conductivity and activation energies.

Sample	ρ_{rel} (%)	S total (S cm^{-1})		Ea (eV)	
		800 °C	600 °C	HT	LT
*P*1	98	6.44×10^{-2}	1.13×10^{-2}	0.71	0.99
*P*2	93	2.47×10^{-2}	3.43×10^{-3}	0.81	0.94
*P*3	93	9.75×10^{-3}	1.79×10^{-3}	0.80	0.89
*P*4	n.d.	5.17×10^{-3}	4.40×10^{-4}	0.92	0.95

ments. When the temperature of formation of the perovskite phase is reached, the side phases are strongly crystallized and hardly react to give the perovskite one. Accordingly, in the case of sample *P*2, notwithstanding the good metal ratios (the lowest ion losses were observed) that would result in a monophasic material, a large amount of side phases was found.

In addition, lower Sr and Mg losses (in *P*2) could have led to an over-stoichiometry of dopants with respect to the solid solubility of SrO and MgO in $LaGaO_3$ at 1400 °C. As a result, the higher doping level could have had a role in the segregation of those amounts of secondary phases.

For what concerns the perovskite phase crystal structure, an interesting parameter to be evaluated is the Goldschmidt tolerance factor, defined as:

$$\tau = \frac{r_A + r_B}{\sqrt{2}\,(r_B + r_O)} \quad (2)$$

where r_A, r_B and r_O are the ionic radii of A-site, B-site and oxygen ions respectively; it is a measure of geometrical distortion of ABO_3-type perovskites, (i.e. its deviation from the ideal cubic structure). The tolerance factor calculated for the refined structures ranges from 0.95 to 1.03 with the minor deviation from the cubic structure ($\tau = 0.995$) belonging to *P*1 and *P*2. For samples *P*1 and *P*2 this small deviation from the cubic structure was also found to be associated with the highest conductivities (discussed in Section 3.4).

3.3. Morphology

Pellets of the final products fired at 1400 °C for 10 h were broken, and the fracture surfaces were observed in an electron microscope (Fig. 7).

Sample *P*1 and *P*2 developed a similar microstructure, with good sintering degree and mean grain sizes in the order of 5–10 μm (inset in Fig. 7a and b). The regularly shaped grains belong to the perovskite phase, while the elongated ones, very frequent in the *P*2 sample, were assigned to the main secondary phase, $LaSrGaO_4$ [44]. In sample *P*3 instead, the microstructure is finer and the mean apparent grain size is below 5 μm (inset in Fig. 7c); nevertheless, the sintering appears good and no porosity is visible. The microstructure appears completely different in *P*4, where large and diffuse porosities are symptom of poor sintering, even if the thermal story is the same for all the samples.

The good sintering and compactness of the sintered pellets, is corroborated by the relative density measurements reported in Table 5, ranging from 93% to 98% of the theoretical ($\rho_{rel}(P1) = 98\%$, $\rho_{rel}(P2) = 93\%$, $\rho_{rel}(P3) = 93\%$). In view of the high porosity (see Fig. 7) the density of *P*4 could not be detected by the Archimede's method.

3.4. Electrical characterization

The electrical properties were determined by Impedance Spectroscopy measurements on sintered pellets. Typical impedance spectra of sample *P*1 at three different temperatures are shown in Fig. 8a. Moving from the higher to lower frequency values, the two arcs represent the contributions relating to the bulk and the grain boundary, respectively, while the electrodes appear as a portion of straight line or an additional arc, depending on the temperature.

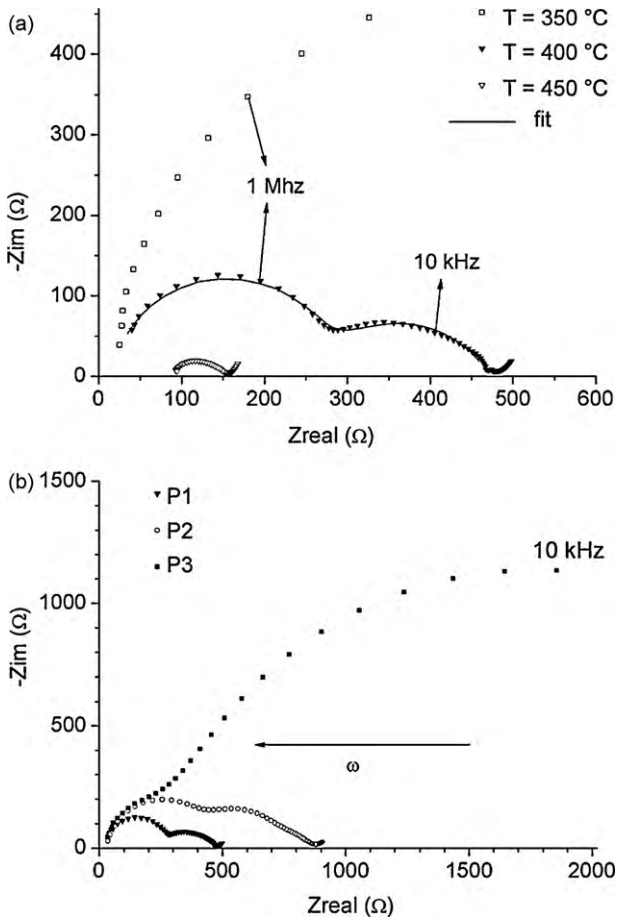

Fig. 8. Nyquist plots of (a) sample *P*1 at $T = 350$, –400 and 450 °C; (b) sample *P*1, *P*2 and *P*3 at $T = 400$ °C.

In fact, it should be remembered that bulk and grain boundary contributes are better resolved at lower temperatures while the electrode contribution is more clearly defined at higher temperatures. In this case ($T \geq 450$ °C), due to very low sample resistance, the bulk semicircle at the highest frequencies is hidden by instrumental effects [45] but its value can be accurately obtained by subtracting the cell impedance from the high frequency intercept of the grain boundary arc. Respect to higher purity LSGM samples obtained with different methods [46], the spectra show the same features with an increase of grain boundary contribute as one can expect due to the presence of larger amount of secondary phases.

Spectra collected at almost the same temperature (around 400 °C) for samples *P*1, *P*2 and *P*3 are shown in Fig. 8b. The identification of the different contributes is difficult due to the presence of several phases and to the lack of the respective conductivity data. For this reason, data will be discussed in term of total conductivity, i.e. the value of the low frequency intercept of the spectrum with the real axis (corrected for the cell resistance). The experimental data can also be fitted by simple equivalent circuits [47]. The IS data were reported in an Arrhenius plot of the total conductivities vs. temperature (Fig. 9). The total conductivities and the apparent activation energies are reported in Table 5. The total conductivities decrease following the sequence $P1 > P2 > P3 > P4$ and are lower than the best value reported in the literature for LSGM ionic conductors (>0.1 S cm^{-1} at 800 °C) [1,4]. *P*1 shows the highest conductivity (0.064 S cm^{-1} at 800 °C), probably due to the coupling of two factors: the relatively low amount of secondary phases (17%) and ion losses (4.6% Ga and 21% Mg); thus, in the end a fairly doped LSGM is obtained. In *P*2 the ion losses are lower, but the high amount

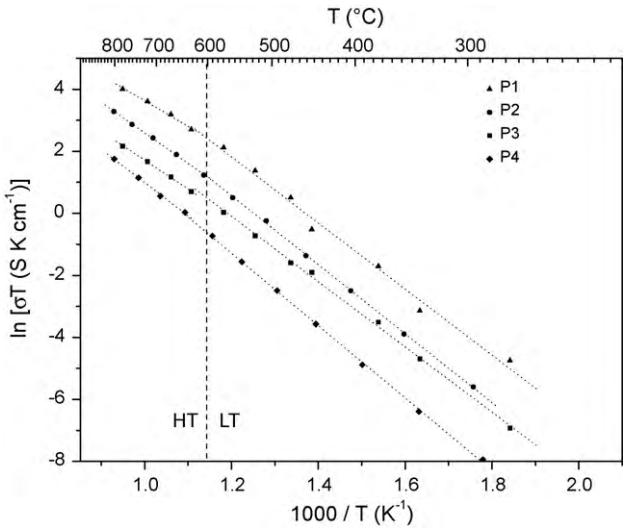

Fig. 9. Arrhenius plots of the total electrical conductivity of *P*1, *P*2, *P*3 and *P*4. HT, high-temperature region; LT, low-temperature region.

of side phases (46%) penalize the conductivity in this case. The low total conductivity of *P*3, although unexpected, arises from the combination of the high loss of dopants (51% and 77% of Sr and Mg respectively, leading to an orthorhombic crystal structure) and from the much finer microstructure where grain boundary density is much higher than in *P*1 and *P*2. In *P*4, again, the perovskite phase obtained is poorly doped and grows in an orthorhombic crystal structure, and has poor electrical conductivity in spite of its single phase composition. The Arrhenius plot was separated in high- (HT, $T > 600\,^{\circ}C$) and low-temperature region (LT, $T < 600\,^{\circ}C$), and activation energies calculated accordingly for two different conduction mechanisms, as commonly accepted for LSGM [4]. The calculated activation energies are similar to those previously reported [4,8], and increase in the high-temperature term in the sequence *P*1 < (*P*2, *P*3) < *P*4.

4. Conclusions

The proposed preparation route, simple and inexpensive, is effective to obtain a final material with LSGM-like structure. However, the control of ions losses during precipitation is the key factor: (i) to avoid the formation of a LSGM phase having a marked distortion from the expected cubic structure and (ii) to prevent the formation of large amounts of secondary phases. In fact, both these deviations from the expected material affect the ionic conductivity.

Slight variations of the co-precipitation procedure can introduce large variations in the final structure, microstructure and phase composition of the sintered samples. Among the studied experimental practices, procedure *P*1, i.e. the use of large excess of $(NH_4)_2CO_3$ precipitating agent, is recommended together with the addition of HNO_3. LSGM with 98% relative density and total conductivities of $6.44 \times 10^{-2}\,S\,cm^{-1}$ at 800 °C and $1.13 \times 10^{-2}\,S\,cm^{-1}$ at 600 °C can be obtained via this route, with a total of 17% of common spurious phases.

Other procedures affect the ions losses and the subsequent development of the final phase leading to an increased amount of secondary phases (total 46% in *P*2, where stoichiometric precipitating agent is used) or to scarcely doped compounds (in *P*3 where HNO_3 was not added, and in *P*4 where NH_4OH was used as precipitating agent).

References

[1] T. Ishihara, H. Matsuda, Y. Takita, J. Am. Chem. Soc. 116 (1994) 3801.
[2] M. Feng, J.B. Goodenough, Eur. J. Solid. State Inorg. Chem. T31 (1994) 663.
[3] M. Rozumek, P. Majewski, F. Aldinger, J. Am. Ceram. Soc. 87 (2004) 656.
[4] K. Huang, K.Q. Huang, R.S. Tichy, J.B. Goodenough, J. Am. Ceram. Soc. 81 (1998) 2565.
[5] E. Djurado, M. Labeau, J. Eur. Ceram. Soc. 18 (1998) 1397.
[6] P. Majewski, M. Rozumek, A.T. Cuneyt, F. Aldinger, J. Electroceram. 8 (2002) 65.
[7] M. Rozumek, P. Majewski, L. Sauter, F. Aldinger, J. Am. Ceram. Soc. 86 (2003) (1940).
[8] K. Huang, M. Feng, J.B. Goodenough, J. Am. Ceram. Soc. 79 (1996) 1100.
[9] K. Huang, J.B. Goodenough, J. Solid State Chem. 136 (1998) 274.
[10] A.T. Cuneyt, P. Majewski, F. Aldinger, J. Am. Ceram. Soc. 83 (2000) 2954.
[11] R. Polini, A. Pamio, E. Traversa, J. Eur. Ceram. Soc. 24 (2004) 1365.
[12] J.W. Stevenson, T.R. Armstrong, L.R. Pederson, J. Li, C.A. Lewinsohn, S. Baskaran, Solid State Ionics 113–115 (1998) 571.
[13] L. Cong, T. He, J. Ji, P. Guan, Y. Huang, W. Su, J. Alloys Compd. 348 (2003) 325.
[14] J.W. Stevenson, T.R. Armstrong, D.E. McCready, L.R. Pederson, W.J. Weber, J. Electrochem. Soc. 144 (1997) 3613.
[15] L.A. Chick, L.R. Pederson, G.D. Maupin, J.L. Bates, L.E. Thomas, G.J. Exarhos, Mater. Lett. 10 (1990) 6.
[16] A. Tarancón, G. Dezanneau, J. Arbiol, F. Peiró, J.R. Morante, J. Power Sources 118 (2003) 256.
[17] M. Shi, N. Liu, Y.D. Xu, Y.P. Yuan, P. Majewski, F. Aldinger, J. Alloys Compd. 425 (2006) 348.
[18] C. Oncel, B. Ozkaya, M.A. Gulgun, J. Eur. Ceram. Soc. 27 (2007) 599.
[19] Z.C. Li, H. Zhang, B. Bergman, X. Zou, J. Eur. Ceram. Soc. 26 (2006) 2357.
[20] M. Kumar, S. Srikanth, B. Ravikumar, T.C. Alex, S.K. Das, Mater. Chem. Phys. 113 (2009) 803.
[21] T.Y. Chen, K.Z. Fung, J. Eur. Ceram. Soc. 28 (2008) 803.
[22] H. Ishikawa, M. Enoki, T. Ishihara, T. Akiyama, J. Alloy Compd. 430 (2007) 246.
[23] J. Chang, H.W. Lee, S.J.L. Kang, J. Am. Ceram. Soc. 92 (2009) 927.
[24] V.P. Gorelov, D.I. Bronin, J.V. Sokolova, H. Nafe, F. Aldinger, J. Eur. Ceram. Soc. 21 (2001) 2311.
[25] P.R. Slater, J.T.S. Irvine, T. Ishihara, Y. Takita, J. Solid State Chem. 139 (1998) 135.
[26] T. Shibasaki, T. Furuya, S. Wang, T. Hashimoto, Solid State Ionics 174 (2004) 193.
[27] M. Kajitani, M. Matsuda, A. Hoshikawa, S. Harjo, T. Kamiyama, I. Toru, F. Izumi, M. Miyake, Chem. Mater. 17 (2005) 4235.
[28] M. Kajitani, M. Matsuda, A. Hoshikawa, S. Harjo, T. Kamiyama, T. Ishigaki, F. Izumi, M. Miyake, J. Phys. Chem. Solids 68 (2007) 758.
[29] L. Vasylechko, V. Vashook, D. Savytskii, A. Senyshyn, R. Niewa, M. Knapp, H. Ullmann, M. Berkowski, A. Matkovskii, U. Bismayer, J. Solid State Chem. 172 (2003) 396.
[30] M.M. Guenter, M. Lerch, H. Boysen, D. Toebbens, E. Suard, C. Baehtz, J. Phys. Chem. Solids 67 (2006) 1754.
[31] P. Datta, P. Majewski, F. Aldinger, J. Alloys Compd. 438 (2007) 232.
[32] M. Kajitani, M. Matsuda, A. Hoshikawa, K.-I. Oikawa, S. Torii, T. Kamiyama, F. Izumi, M. Miyake, Chem. Mater. 15 (2003) 3468.
[33] A. Skowron, P.-N. Huang, A. Petric, J. Solid State Chem. 143 (1999) 202.
[34] Y. Idemoto, T. Sugiyama, N. Kitamura, T. Itoh, Electrochemistry 77 (2009) 152.
[35] G. Groppi, M. Bellotto, C. Cristiani, P. Forzatti, J. Mater. Sci. 29 (1994) 3441.
[36] P.S. Cho, S.Y. Park, Y.H. Cho, S.J. Kim, Y.C. Kang, T. Mori, J.H. Lee, Solid State Ionics 180 (2009) 788.
[37] N.S. Chae, K.S. Park, Y.S. Yoon, I.S. Yoo, J.S. Kim, H.H. Yoon, J. Colloid Surf. A 154 (2008) 313.
[38] C. Cristiani, L. Zampori, S. Latorrata, R. Pelosato, G. Dotelli, R. Ruffo, Mater. Lett. 63 (2009) 1892.
[39] P.-S. Cho, S.-Y. Park, Y.H. Cho, S.-J. Kim, Y.C. Kang, T. Mori, J.-H. Lee, Solid State Ionics 180 (2009) 788.
[40] H. M. Rietveld, J. Appl. Crystallogr. 2 (1969) 65, using the program GSAS written by A.C. Larson, R.B. Von Dreele, General Structure Analysis System, Los Alamos National Laboratory Report LA-UR-86-748, 2000.
[41] F. Zheng, Y. Chen, J. Mater. Sci. 43 (2008) 2058.
[42] K. Yamaji, T. Horita, M. Ishikawa, N. Sakai, H. Yokokawa, Solid State Ionics 108 (1998) 415.
[43] K. Nakamoto, Infrared Spectra of Inorganic and Coordination Compounds, Wiley & Sons, New York, 1963.
[44] K. Furuya, M. Hatano, K. Fujii, United States Patent US 7,205,063 B2, April 2007.
[45] B. Buokamp, Solid State Ionics 62 (1993) 131.
[46] I. Natali Sora, R. Pelosato, G. Dotelli, C. Schmid, R. Ruffo, C.M. Mari, Solid State Ionics 176 (2004) 81.
[47] R. Pelosato, I. Natali Sora, G. Dotelli, R. Ruffo, C.M. Mari, Solid State Ionics 177 (2006) 1991.